LAWRENCE
LIVERMORE
NATIONAL
LABORATORY

LLNL-JRNL-839029

Tip-enhanced second harmonic generation microscopy for nanoscale chemical imaging

Y. Rho, S. Yoo, D. Durham, A. M. Minor, H. K. Park, C. P. Grigoropoulos

August 22, 2022

Nano Letters

Abstract

Nonlinear optical response is a fingerprint of various physicochemical properties of materials related to symmetry, including crystallography, interfacial status, and carrier dynamics. However, the intrinsically weak nonlinear optical susceptibility and the diffraction limit of far-field optics restrict probing deep-subwavelength scale nonlinear optics with measurable signal-to-noise ratio. Here, we propose an alternative approach toward efficient second harmonic generation (SHG) nanoscopy for SHG-active sample (zinc oxide nanowire (ZnO NW)) using an SHG-active plasmonic nanotip. Our full-wave simulation suggests that the experimentally observed high near-field SHG contrast is possible when the nonlinear response of ZnO NW is enhanced and/or that of the tip is suppressed. This result suggests possible evidence of quantum mechanical nonlinear energy transfer (NET) between the tip and the sample, modifying the nonlinear optical susceptibility. Further, this process probes the nanoscale corrosion of ZnO NW, demonstrating potential use in studying various physicochemical phenomena in nanoscale resolution.

Keywords: Nonlinear optics, Second harmonic generation (SHG), Near-field optics, Zinc oxide nanowire

Introduction

Symmetry in the material structures, *e.g.*, crystal structures and surface/interface, and the induced electromagnetic fields determines optical nonlinearity of the material. For example, SHG, one of the second-order nonlinear optical responses, typically occurs when the material of interest and/or induced electromagnetic field distribution lacks inversion symmetry[1-8]. This characteristic of SHG offers a powerful pathway to studying crystallography[2], interfacial status[3, 4], optical resonance[5-7], and carrier dynamics[8] of various material systems. However, intrinsically weak nonlinear optical signals and limited resolution by far-field optical configuration require additional strategy to accomplish nanoscale detection at a measurable signal-to-noise ratio.

A nanoimaging of nonlinear optical properties was firstly demonstrated by introducing nano-aperture that physically confines region for photon collection[9-13]. Meanwhile, apertureless type plasmonic nanoscopic tip has been introduced by virtue of its strong near-field amplification with relatively free of constraints on polarization and geometric configuration[14-19]. For example, plasmonic grooved tips[17, 18], and tip tilting[19] have been introduced to improve the nonlinear optical contrast by improving light coupling efficiency at the tip apex. Meanwhile, the plasmonic enhancement at the metallic tip apex inevitably generates tip-induced local SH photons[15, 18-21], which are often deemed undesirable in SHG studies as it can degrade the signal-to-noise ratio. In such plasmonic tip-based near-field SHG techniques, it is ambiguous whether the measured signals track the sample SHG responses since both the sample and the tip contribute simultaneously. Also, quantum mechanical effects may modify the SH susceptibility of the sample and/or the tip[22-24], making the interpretation of near-field SHG data complicated. These imply that new pathways in nanoscale amplification and probing of nonlinear optical properties of materials can be possible, expanding applications of the tip enhanced SHG nanoscopy.

Here, we demonstrate nanoscale imaging of near-field SHG using a SHG-active plasmonic gold (Au) nanotip. The Au tip not only provides the plasmonic field enhancement demonstrated in previous reports[15, 16, 19], but also has its own SHG response that boosts the SHG signals of the target sample. ZnO NW is chosen as the SHG-active target sample because of their low refractive index contrast compared to the substrate, which allows us to exclude other linear optical effects in our SHG nanoscopy imaging. We suggest that our observed high signal contrast can be possible through quantum mechanical NET between the Au tip and the sample. We achieved clear near-field contrast with nanoscale resolution (<13 nm) from ZnO NW at the SH frequency. Further, we apply our method to nanoscale characterization of local corrosion of ZnO NW. Our work offers a promising way to future study of various physicochemical phenomena in nanoscale resolution.

Results and Discussion

- Experimental observation of near-field SHG contrast from ZnO NW

Fig. 1a schematically shows the tip-enhanced near-field SHG nanoimaging. We utilize an Au-coated Si tip (apex radius of ~30 nm) as an optical probe. Although the Au-coated tip itself is SHG-active even in free space, here we utilize the SHG response of the Au-coated tip to spatially map the near-field SHG response of the sample with strong contrast via NET between the tip and the sample, a mechanism that will be discussed later in detail. To induce SHG response of the tip during the near-field mapping, we illuminate a femtosecond laser beam (λ_0~810 nm, f~80 MHz, pulse duration~100 fs) on the tip apex (Fig. 1a). Since the tip points in the direction normal to the substrate, p-polarized illumination can induce strong SHG signals from the tip-apex. This can be shown in the SHG intensity mapping image of the tip apex (inset image of Fig. 1b) obtained by

scanning the laser around the tip while collecting the SHG photons by a photon counter (Supporting Note 1).

We test our approach for the near-field SHG mapping using Wurtzite ZnO NWs, drop-casted on a SiO_2 (300 nm)/Si substrate. We choose ZnO NW as its broken inversion symmetry produces distinct SHG signals[25, 26], while having small contrast of refractive index (n_{ZnO}=1.60) compared to the substrate (n_{SiO2}=1.45) both at the fundamental frequency (λ_0=810 nm) and at the SH frequency (λ_{SHG}=405 nm). This small dielectric contrast of the ZnO NW sample makes us possible to exclude the linear effect on the measured near-field SHG imaging. ZnO NW is also one of the most studied nanomaterials owing to its rich electrochemical properties, biocompatibility, and intrinsically stable oxide stoichiometries[27, 28]. High-resolution transmission electron microscopy (HRTEM) (Fig. 1f), combined with selected area electron diffraction (SAED) pattern analysis (Fig. 1e) confirms these are single crystal ZnO NWs in a Wurtzite crystal structure[29]. The polarization resolved far-field SHG pattern shows two-lobed shape, confirming its *6mm* point group with the non-zero SH susceptibilities[25, 26] (Supporting Note 3).

We first spatially image the tip-enhanced near-field SHG response from ZnO NW (Fig. 2b) by collecting the SH photons while scanning the tip. During the scanning, the average distance between the tip apex and the sample is maintained at 2 nm (Supporting Note 1). We observe clear near-field SHG contrast ($\equiv \left(I_{SHG,ZnO} - I_{SHG,subs}\right)/I_{SHG,subs}$) of 0.7-2.5, from ZnO NW with various thicknesses (90-170 nm) (Fig. 2c). The near-field SHG signal follows well the topography with nanoscale resolution ~13 nm ($\sim(FWHM_{Topography}\text{-}FWHM_{SHG})/2$) (Supporting Note 4).

The experimentally observed near-field SHG contrast implies complicated physics beyond classical understanding. As we mentioned, it is not likely that the small refractive index contrast

between the sample (n_{ZnO}=1.60) and the substrate (n_{SiO2}=1.45) can induce the observed high near-field SHG contrast in Fig. 2b. To investigate the origin of the strong contrast further, we also study the tip-height dependence of the SHG intensity signals from the ZnO NW and the SiO_2/Si substrate that exhibit different trends (Fig. 2d). As we lift the tip from the sample, the measured SHG intensity from the ZnO NW monotonically decreases and appears to saturate after ~50 nm of tip-sample distance, whereas if the tip probes the SiO_2/Si substrate, the SHG intensity gradually increases up to ~100 nm of tip-sample distance. The trend of the SHG intensity on the bare substrate (blue dots in Fig. 2d) is straightforward to understand; the SiO_2 layer of the substrate is SHG-inactive, and thus the SHG intensity is proportional to the field intensity at the tip position at the fundamental frequency. Since the light reflected back by the SiO_2/Si substrate interferes with the incident light of the wavelength 810 nm and the incident angle 60°, the interference pattern of the field intensity follows the trend of $\sin^2(k_{0,z}\, z)$ with the normal component of the wave vector at the fundamental frequency, $k_{0,z}=(2\pi/\lambda_0)\sin(60°)$ as shown in the simulated electromagnetic field distribution in Fig. S6. On SHG-active ZnO NW, however, the SHG intensity on the ZnO NW sample shows significantly different trend compared to that on the bare substrate (Fig. 2d). We hypothesize that the tip-sample interaction is mediated by the evanescent field. Note that exponentially decaying interaction scaling with respect to the distance can be found in other interactions mediated by the evanescent fields, *e.g.* Au NP-fluorescent molecule interaction[30], the fluorescence resonant energy transfer (FRET)[31], and plasmonic molecular rulers[32]. We fit the experimentally measured SHG intensity on the ZnO NW sample using $\exp(-4\pi z/d_{int})$, yielding the interaction constant d_{int}=405 nm (Fig. 2d), which is the same as the wavelength of the SH frequency. This coincidence may suggest that the tip-sample interaction is mediated by the evanescent near-field at the SH frequency.

- **Theoretical interpretation of the observed near-field SHG enhancement from ZnO NW**

To understand our experimental observation of the near-field SHG mapping, we investigated three possible explanations theoretically; (i) The Au-coated tip induces strong near-field in its vicinity because Au supports surface plasmons at λ_0=810 nm. Classically, this strong near-field enhancement at the fundamental frequency becomes source at the SH frequency, yielding the strong near-field SHG of the ZnO NW. (ii) It has been known that the Purcell effect, a resonator-induced modification of spontaneous decay rate of an emitter, can perturb the nonlinear susceptibility of materials[22-24]. (iii) We also conjecture that the quantum mechanical NET can modify the nonlinear susceptibilities of Au and/or ZnO if two materials are coupled strongly.

To examine the first explanation offered, we numerically solve the Maxwell's equations, which describe classical electrodynamics phenomena, at the fundamental and the SH frequencies in a self-consistent manner using the reported nonlinear susceptibilities[25, 33] (Supporting Note 5). Based on the simulated electromagnetic fields $\left\{\mathbf{E}^{(2\omega)}(\mathbf{r}), \mathbf{H}^{(2\omega)}(\mathbf{r})\right\}$ at the SH frequency, we define SH-cross section (SH-CS), the surface-integration of the outgoing Poynting vector normal to an arbitrary surface enclosing the tip and the sample, *i.e.* $C_{sca}^{(2\omega)} \equiv -Re \oiint \left(\boldsymbol{E}^{(2\omega)} \times \boldsymbol{H}^{(2\omega)}\right) \cdot d\boldsymbol{a} \,/\, \left(2I_0^{(\omega)}\right)$, where $I_0^{(\omega)}$ is the intensity of the incident wave at ω. Most strikingly, our numerical simulation shows the tip SHG intensity dominates the sample SHG intensity of ZnO NW (Supporting Note 6). The SH-CS on ZnO NW ($C_{sca,ZnO}^{(2\omega)}$) exhibits an interference pattern (Fig. S7a), contrasting with our experimental observation in Fig. 2d. In addition, the near-field SHG contrast ($\equiv \left(C_{sca,ZnO}^{(2\omega)} - C_{sca,subs}^{(2\omega)}\right)/C_{sca,subs}^{(2\omega)}$) is 0.18, when the tip approaches the ZnO NW surface at a distance of 5 nm (Fig. S7b), which is much smaller than the experimentally observed near-field

SHG contrast (0.7-2.5). Therefore, we can exclude the classical effect for explaining our experimental findings.

Second, we consider the Purcell effect-modification of the nonlinear susceptibilities of the Au-coated tip and the ZnO NW. SHG is a three-level process where a transition from the highest virtual state to the ground state causes SHG at the SH frequency, while the transitions from the first excited state to the ground state describe the linear response at the fundamental frequency[1]. If an optical resonator possesses a small local density of states (LDOS), *i.e.*, a Purcell factor lower than unity, the transitions at the first excited state are suppressed[22-24]. This would induce more transitions from the highest virtual state at the SH frequency, hence enhancing the nonlinear SH susceptibility. However, our Au-coated tip has large LDOS due to strong plasmonic response at λ_0=810 nm (Supporting Note 7). In this electromagnetic configuration, nonlinear susceptibilities of both Au and ZnO are suppressed, contrasting with our experimental findings.

As we have seen, the first two well-known scenarios (*i.e.*, classical plasmonic field enhancement and the Purcell effect-induced nonlinear susceptibility modification) fail to explain our experimental findings. Then, we hypothesize that energy transfer between Au and ZnO occurs in SHG process as shown in Figs. 3a&b. This is analogous to FRET between two fluorescent systems[34]. In a FRET system, fluorescence of one emitter can be enhanced while that of another emitter is suppressed while providing energy to the enhanced emitter. If a similar energy transfer can occur in the coupled SHG-active system (Fig. 3b), the nonlinear susceptibility of the Au-coated tip can be enhanced while that of the ZnO NW is suppressed, or *vice versa*. We coin the term, nonlinear energy transfer (NET), for this effect. Although ultrafast nonlinear spectroscopy to confirm NET exclusively is beyond our scope, we find possible evidence of NET from dependence of SHG intensity on the tip-sample distance. We perform the numerical simulations with

artificially controlled nonlinear SH polarizations; the SH polarization of ZnO $\boldsymbol{P}_{ZnO}^{(2\omega)}$ (Au, surface and bulk components $\boldsymbol{P}_{Au,bulk}^{(2\omega)}$ and $\boldsymbol{P}_{Au,surf}^{(2\omega)}$) is modified by a factor f_{ZnO} (f_{Au}) compared to the uncoupled SH polarization $\boldsymbol{P}_{ZnO,0}^{(2\omega)}$ ($\boldsymbol{P}_{Au,bulk,0}^{(2\omega)}$ and $\boldsymbol{P}_{Au,surf,0}^{(2\omega)}$), *i.e.* $\boldsymbol{P}_{ZnO}^{(2\omega)} = f_{ZnO}\boldsymbol{P}_{ZnO,0}^{(2\omega)}$ ($\boldsymbol{P}_{Au,bulk}^{(2\omega)} = f_{Au}\boldsymbol{P}_{Au,bulk,0}^{(2\omega)}$ and $\boldsymbol{P}_{Au,surf}^{(2\omega)} = f_{Au}\boldsymbol{P}_{Au,surf,0}^{(2\omega)}$).

In Fig. 3c, we increase f_{ZnO} from 1 to 100, while f_{Au} is fixed to the unity and plot the normalized SH-CS of the Au tip according to the tip-sample distance. This represents the enhancement of ZnO-SHG while Au-SHG remains the same. As also shown in Fig. 3d, the tip-sample distance dependence becomes significantly different. For f_{ZnO}=1, SH-CS is dominated by Au-SHG, increasing with the tip-sample distance, which indicates interference pattern while ZnO-SHG cannot be resolved. However, as f_{ZnO} increases, ZnO-SHG starts to dominate, and the case when f_{ZnO} is much higher than f_{Au} (*i.e.*, f_{ZnO}=100) shows an identical SH-CS trend to the case when only ZnO-SHG is considered (*i.e.*, f_{Au}=0). In both cases, SH-CS becomes flat for large tip-sample distance (>30 nm), which is consistent with our experimental finding in Fig. 2d, indicating that the enhancement of ZnO-SHG can reproduce our experimental result. We also test the opposite scenario, *i.e.* the quenching of Au-SHG with the fixed ZnO-SHG (decreasing f_{Au} with the fixed f_{ZnO}=1), and the result reproduces the experimental observation when f_{Au} is much smaller than f_{ZnO}. We conclude that our nonlinear near-field mapping experiment could originate from the combination of the enhanced $\boldsymbol{P}_{ZnO}^{(2\omega)}$ and/or the quenched $\boldsymbol{P}_{Au}^{(2\omega)}$. To complement, we also calculate a nonlinear susceptibility of coupled anharmonic oscillators (Supporting Note 8), and it shows the modification of $\boldsymbol{P}_{ZnO}^{(2\omega)}$ and quenched $\boldsymbol{P}_{Au}^{(2\omega)}$ is possible even for weak coupling constant g.

- **Nanoscale corrosion imaging of ZnO NW**

Our experimental and theoretical studies suggest that the tip-enhanced near-field SHG nanoscopy can sensitively probe the local nonlinear susceptibility of ZnO NW crystals with nanoscale resolution. We explore the potential use of this technique in nanoimaging of the corrosion process of ZnO NW. Although ZnO NW has been considered as a chemically stable material, previous studies revealed that it can degrade by exposure to ambient molecules such as H_2O and CO_2[35-38]. We induce corrosion in ZnO NW by exposure to high relative humidity (RH at 90%) environment for two days. Prominent corrosion is manifested by bubbled structure with etched pits (Fig. 4a). HRTEM image obtained from the bubble shows that it is comprised of nanocrystals (Fig. 4c), and the ring pattern observed in SAED (Fig. 4d) confirms the polycrystalline nature with d-spacings that are consistent with Wurtzite ZnO. Energy-dispersive x-ray spectroscopy (EDS) shows that the elemental ratios of O to Zn (O/Zn) from the bubble structure and ZnO NW backbone are in similar range, 1.3 and 1.2, respectively (Supporting Note 10). This ratio is close to the stoichiometry of ZnO, while the slight increase in oxygen can be attributed to residues from hydroxyl groups from the water as well as adsorbed and deposited organic contaminants from air. We attribute this corrosion process to water induced etching and recrystallization, preferentially initiated at oxygen vacancy sites[37, 39] (Supporting Note 11).

The tip-enhanced near-field SHG microscopy can effectively probe the observed corrosion process with nanoscale resolution. We performed near-field SHG imaging of the ZnO NW after the corrosion process (Figs. 4e&f). The corroded ZnO NW shows dramatically different topography and near-field SHG distribution compared to the pristine ZnO NW (Figs. 2a&b). The local near-field SHG intensity is stronger at the thinner area, while decreased intensity is measured in the thicker area. As previously discussed, the observed signal contrast may be attributed to the distance sensitive near-field SHG process by NET we suggested. The vertical growth of polycrystalline

ZnO in the bubbled region increases the distance between the tip and the pristine ZnO NW backbone. This minimizes the tip-crystalline ZnO NW interaction, whereas SHG emission from polycrystalline ZnO is minimal due to the random crystal orientation of each particle. In contrast, the tip apex can access the pristine ZnO NW core in thinner and uncorroded regions where stronger SHG intensity can be induced. In heavily degraded ZnO NW (Figs. 4g&h), the near-field SHG signal diminishes due to the thick corroded by-product. In contrast, the far-field SHG is also captured as a uniform tail-like interference pattern outside ZnO NW (Fig. 4h). This far-field SHG indicates the existence of unaffected ZnO crystals in the deep core area inside the corroded region; the incident plane wave excites the core crystalline ZnO NW, and then the far-field SHG are captured by the Au tip, which is away from ZnO NW. Thus, this result shows that our method can sensitively monitor the progress of non-uniform surface status of nanomaterials in nanoscale resolution.

Conclusion

In summary, we demonstrate nanoscale tip-enhanced near-field SHG probing of ZnO NWs. We experimentally observe near-field SHG signal from ZnO NW with high signal-to-noise ratio at high resolution (<13 nm). We propose that the strong SHG response of Au tips can be used as an optical probe for acquiring SHG signals from nonlinear samples. In the system examined, this possibly originates from a NET between the tip and the ZnO NW in a nonlinear process, while neither the plasmonic field enhancement nor the Purcell effect can explain the experimentally observed SHG enhancement. We further show that near-field SHG can be applied to probe the corrosion process of ZnO NWs. We believe that the proposed approach by NET promotes future

study of nanoscale nonlinear optical properties of various material systems, enabling promising applications in electrochemistry and optoelectronics.

Experimental Methods

- **Tip enhanced near-field SHG nanoscopy system:**

Details are described in Supporting Note 1.

- **ZnO NW sample preparation and corrosion process:**

CVD grown ZnO NW is purchased from Novarials, USA. The NWs are suspended in isopropyl alcohol (IPA) and drop casted on SiO_2 (300 nm)/Si wafer. The corrosion process is performed by placing ZnO NW under the high relative humidity (>90%) for two days.

- **TEM analysis:**

HRTEM, SAED, and EDS are performed on an FEI TitanX using 300 kV beam voltage. ZnO NWs are drop cast on commercially available holey silicon nitride membrane windows for TEM (Norcada). A TEM chip with deposited NWs is included with the wafer being corroded to experience the same conditions. NWs with less than 100 nm width and regions that extend over holes in the membrane are chosen for analysis to reduce thickness effects and avoid contributions from the silicon nitride. EDS quantification is performed using the Bruker ESPRIT software package.

- **Numerical simulations and development of theoretical models**

Details are described in Supporting Notes 5-8.

Acknowledgements: Y. Rho and S. Yoo equally contributed to this work. Financial support awarded to the Laser Prismatics LLC., and University of California, Berkeley, by the U.S. Department of Energy (Grant No. SBIR/STTR DE-SC0018461) is gratefully acknowledged. Work at the Molecular Foundry was supported by the Office of Science, Office of Basic Energy Sciences, of the U.S. Department of Energy under Contract No. DE-AC02-05CH11231. S. Yoo was supported by the National Research Foundation of Korea (NRF) grant funded by the Korea government (MSIT) (No. NRF-2022R1F1A1074019). Part of this work by Y.R. was performed under the auspices of the U.S. Department of Energy by Lawrence Livermore National Laboratory under Contract DE-AC52-07NA27344. We also thank Dr. S. Park, Dr. T. Albrecht, and Dr. D. Nowak at Molecular Vista for useful discussions on system development. **Conflicts of Interest:** The authors declare no competing financial interest.

References

1. Boyd, R. W., *Nonlinear optics*. Academic press: 2020.

2. Denev, S. A.; Lummen, T. T.; Barnes, E.; Kumar, A.; Gopalan, V., Probing ferroelectrics using optical second harmonic generation. *Journal of the American Ceramic Society* **2011,** *94* (9), 2699-2727.

3. Corn, R. M.; Higgins, D. A., Optical second harmonic generation as a probe of surface chemistry. *Chemical reviews* **1994,** *94* (1), 107-125.

4. Tran, R. J.; Sly, K. L.; Conboy, J. C., Applications of surface second harmonic generation in biological sensing. *Annual Review of Analytical Chemistry* **2017,** *10*, 387-414.

5. Makarov, S. V.; Petrov, M. I.; Zywietz, U.; Milichko, V.; Zuev, D.; Lopanitsyna, N.; Kuksin, A.; Mukhin, I.; Zograf, G.; Ubyivovk, E.; Smirnova, D. A.; Starikov, S.; Chichkov, B. N.; Kivshar, Y. S., Efficient Second-Harmonic Generation in Nanocrystalline Silicon Nanoparticles. *Nano Letters* **2017,** *17* (5), 3047-3053.

6. Butet, J.; Brevet, P.-F.; Martin, O. J., Optical second harmonic generation in plasmonic nanostructures: from fundamental principles to advanced applications. *ACS nano* **2015,** *9* (11), 10545-10562.

7. Grinblat, G.; Rahmani, M.; Cortés, E.; Caldarola, M.; Comedi, D.; Maier, S. A.; Bragas, A. V., High-efficiency second harmonic generation from a single hybrid ZnO nanowire/Au plasmonic nano-oligomer. *Nano letters* **2014,** *14* (11), 6660-6665.

8. Tisdale, W. A.; Williams, K. J.; Timp, B. A.; Norris, D. J.; Aydil, E. S.; Zhu, X.-Y., Hot-Electron Transfer from Semiconductor Nanocrystals. *Science* **2010,** *328* (5985), 1543-1547.

9. Zayats, A. V.; Kalkbrenner, T.; Sandoghdar, V.; Mlynek, J., Second-harmonic generation from individual surface defects under local excitation. *Physical Review B* **2000,** *61* (7), 4545-4548.

10. Johnson, J. C.; Yan, H.; Schaller, R. D.; Petersen, P. B.; Yang, P.; Saykally, R. J., Near-Field Imaging of Nonlinear Optical Mixing in Single Zinc Oxide Nanowires. *Nano Letters* **2002,** *2* (4), 279-283.

11. Schaller, R. D.; Johnson, J. C.; Saykally, R. J., Time-Resolved Second Harmonic Generation Near-Field Scanning Optical Microscopy. *ChemPhysChem* **2003,** *4* (11), 1243-1247.

12. Zavelani-Rossi, M.; Celebrano, M.; Biagioni, P.; Polli, D.; Finazzi, M.; Duò, L.; Cerullo, G.; Labardi, M.; Allegrini, M.; Grand, J.; Adam, P.-M., Near-field second-harmonic generation in single gold nanoparticles. *Applied Physics Letters* **2008,** *92* (9), 093119.

13. Celebrano, M.; Biagioni, P.; Zavelani-Rossi, M.; Polli, D.; Labardi, M.; Allegrini, M.; Finazzi, M.; Duò, L.; Cerullo, G., Hollow-pyramid based scanning near-field optical microscope

coupled to femtosecond pulses: A tool for nonlinear optics at the nanoscale. *Review of Scientific Instruments* **2009,** *80* (3), 033704.

14. Zayats, A. V.; Sandoghdar, V., Apertureless scanning near-field second-harmonic microscopy. *Optics communications* **2000,** *178* (1-3), 245-249.

15. Neacsu, C. C.; van Aken, B. B.; Fiebig, M.; Raschke, M. B., Second-harmonic near-field imaging of ferroelectric domain structure of YMnO 3. *Physical Review B* **2009,** *79* (10), 100107.

16. Cimatu, K. A.; Mahurin, S. M.; Meyer, K. A.; Shaw, R. W., Nanoscale chemical imaging of zinc oxide nanowire corrosion. *The Journal of Physical Chemistry C* **2012,** *116* (18), 10405-10414.

17. Jiang, T.; Kravtsov, V.; Tokman, M.; Belyanin, A.; Raschke, M. B., Ultrafast coherent nonlinear nanooptics and nanoimaging of graphene. *Nature Nanotechnology* **2019,** *14* (9), 838-843.

18. Berweger, S.; Atkin, J. M.; Olmon, R. L.; Raschke, M. B., Light on the Tip of a Needle: Plasmonic Nanofocusing for Spectroscopy on the Nanoscale. *The Journal of Physical Chemistry Letters* **2012,** *3* (7), 945-952.

19. Park, K.-D.; Raschke, M. B., Polarization control with plasmonic antenna tips: a universal approach to optical nanocrystallography and vector-field imaging. *Nano letters* **2018,** *18* (5), 2912-2917.

20. Neacsu, C. C.; Reider, G. A.; Raschke, M. B., Second-harmonic generation from nanoscopic metal tips: Symmetry selection rules for single asymmetric nanostructures. *Physical Review B* **2005,** *71* (20), 201402.

21. Bouhelier, A.; Beversluis, M.; Hartschuh, A.; Novotny, L., Near-Field Second-Harmonic Generation Induced by Local Field Enhancement. *Physical Review Letters* **2003,** *90* (1), 013903.

22. Bermel, P.; Rodriguez, A.; Joannopoulos, J. D.; Soljačić, M., Tailoring optical nonlinearities via the Purcell effect. *Physical review letters* **2007,** *99* (5), 053601.

23. Evangelou, S., Tailoring second-order nonlinear optical effects in coupled quantum dot-metallic nanosphere structures using the Purcell effect. *Microelectronic Engineering* **2019,** *215*, 111019.

24. Lin, Z.; Liang, X.; Lončar, M.; Johnson, S. G.; Rodriguez, A. W., Cavity-enhanced second-harmonic generation via nonlinear-overlap optimization. *Optica* **2016,** *3* (3), 233-238.

25. Liu, C.; Zhang, B.; Binh, N.; Segawa, Y., Second harmonic generation in ZnO thin films fabricated by metalorganic chemical vapor deposition. *Optics communications* **2004,** *237* (1-3), 65-70.

26. Larciprete, M. C.; Centini, M., Second harmonic generation from ZnO films and nanostructures. *Applied Physics Reviews* **2015,** *2* (3), 031302.

27. Ozgur, U.; Hofstetter, D.; Morkoc, H., ZnO devices and applications: a review of current status and future prospects. *Proceedings of the IEEE* **2010,** *98* (7), 1255-1268.

28. Kołodziejczak-Radzimska, A.; Jesionowski, T., Zinc oxide—from synthesis to application: a review. *Materials* **2014,** *7* (4), 2833-2881.

29. Aminoff, G., XXIV. Über Lauephotogramme und Struktur von Zinkit. *Zeitschrift für Kristallographie - Crystalline Materials* **1921,** *56* (1-6), 495-505.

30. Anger, P.; Bharadwaj, P.; Novotny, L., Enhancement and Quenching of Single-Molecule Fluorescence. *Physical Review Letters* **2006,** *96* (11), 113002.

31. Ray, P. C.; Fan, Z.; Crouch, R. A.; Sinha, S. S.; Pramanik, A., Nanoscopic optical rulers beyond the FRET distance limit: fundamentals and applications. *Chemical Society Reviews* **2014,** *43* (17), 6370-6404.

32. Sönnichsen, C.; Reinhard, B. M.; Liphardt, J.; Alivisatos, A. P., A molecular ruler based on plasmon coupling of single gold and silver nanoparticles. *Nature Biotechnology* **2005,** *23* (6), 741-745.

33. Krause, D.; Teplin, C. W.; Rogers, C. T., Optical surface second harmonic measurements of isotropic thin-film metals: Gold, silver, copper, aluminum, and tantalum. *Journal of applied physics* **2004,** *96* (7), 3626-3634.

34. Colas des Francs, G.; Girard, C.; Martin, O. J. F., Fluorescence resonant energy transfer in the optical near field. *Physical Review A* **2003,** *67* (5), 053805.

35. Pan, Z.; Tao, J.; Zhu, Y.; Huang, J.-F.; Paranthaman, M. P., Spontaneous growth of ZnCO3 nanowires on ZnO nanostructures in normal ambient environment: unstable ZnO nanostructures. *Chemistry of Materials* **2010,** *22* (1), 149-154.

36. Falk, T.; Svensson, J. E.; Johansson, L. G., The role of carbon dioxide in the atmospheric corrosion of zinc: a laboratory study. *Journal of the Electrochemical Society* **1998,** *145* (1), 39.

37. Milano, G.; D'Ortenzi, L.; Bejtka, K.; Mandrile, L.; Giovannozzi, A. M.; Boarino, L.; Pirri, C. F.; Ricciardi, C.; Porro, S., Tuning ZnO nanowire dissolution by electron beam modification of surface wetting properties. *The Journal of Physical Chemistry C* **2018,** *122* (14), 8011-8021.

38. Zhou, J.; Xu, N. S.; Wang, Z. L., Dissolving behavior and stability of ZnO wires in biofluids: a study on biodegradability and biocompatibility of ZnO nanostructures. *Advanced Materials* **2006,** *18* (18), 2432-2435.

39. Ali, M.; Winterer, M., ZnO nanocrystals: surprisingly 'alive'. *Chemistry of Materials* **2010,** *22* (1), 85-91.

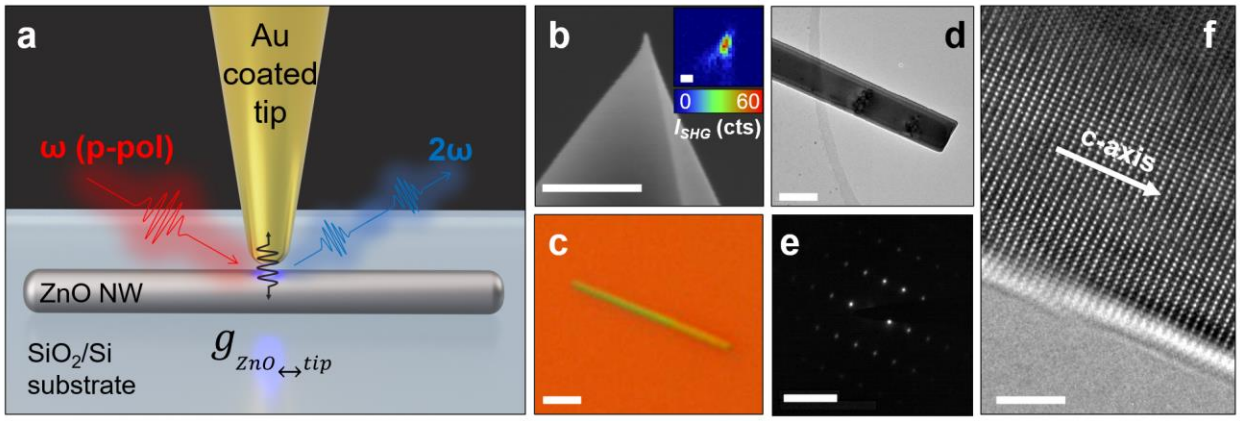

Figure 1: a) Schematics of tip-enhanced near-field SHG imaging of ZnO NW with Au coated tip. b) SEM image of the tip and the SHG intensity (I_{SHG}) mapping image of the tip (inset) obtained by scanning the femtosecond laser around the tip while collecting SHG photons by a photon counter. The scale bars indicate 1 μm. c) Optical microscope image of pristine ZnO NW. The scale bar indicates 5 μm. d-f) Transmission electron microscopy (TEM) analysis of pristine ZnO NW observed along [1 -1 0]: d) low-resolution TEM image, e) selected area electron diffraction (SAED) pattern, and f) high resolution (HR)TEM image showing Wurtzite crystal structure grown along the c-axis with c lattice parameter equal to 5.2 nm. The white arrow in panel f) indicates c-axis crystal orientation of ZnO NW. The scale bars in panels d), e) and f) are 100 nm, 10 1/nm and 2 nm, respectively.

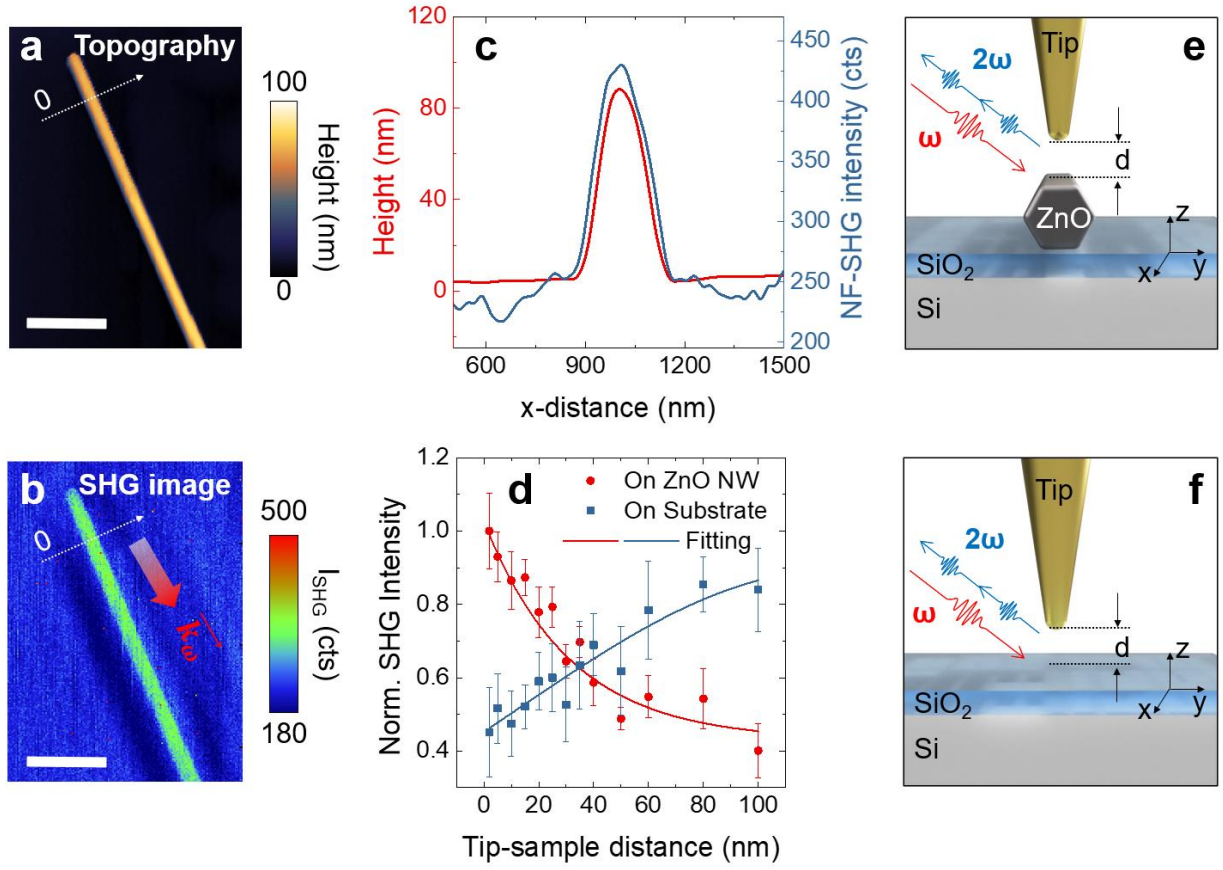

Figure 2: Experimental results on tip-enhanced near-field SHG nanoscopy of ZnO NW. a) Topography and b) near-field SHG image of pristine ZnO NW. The scale bars are 1 μm. c) Line profiles of topography and near-field SHG of ZnO NW obtained from the white dashed lines in panels a) and b). d) Normalized SHG intensity versus tip-sample distance curves obtained from on ZnO NW and on SiO_2/Si substrate, which are schematically depicted in panels e) and f), respectively.

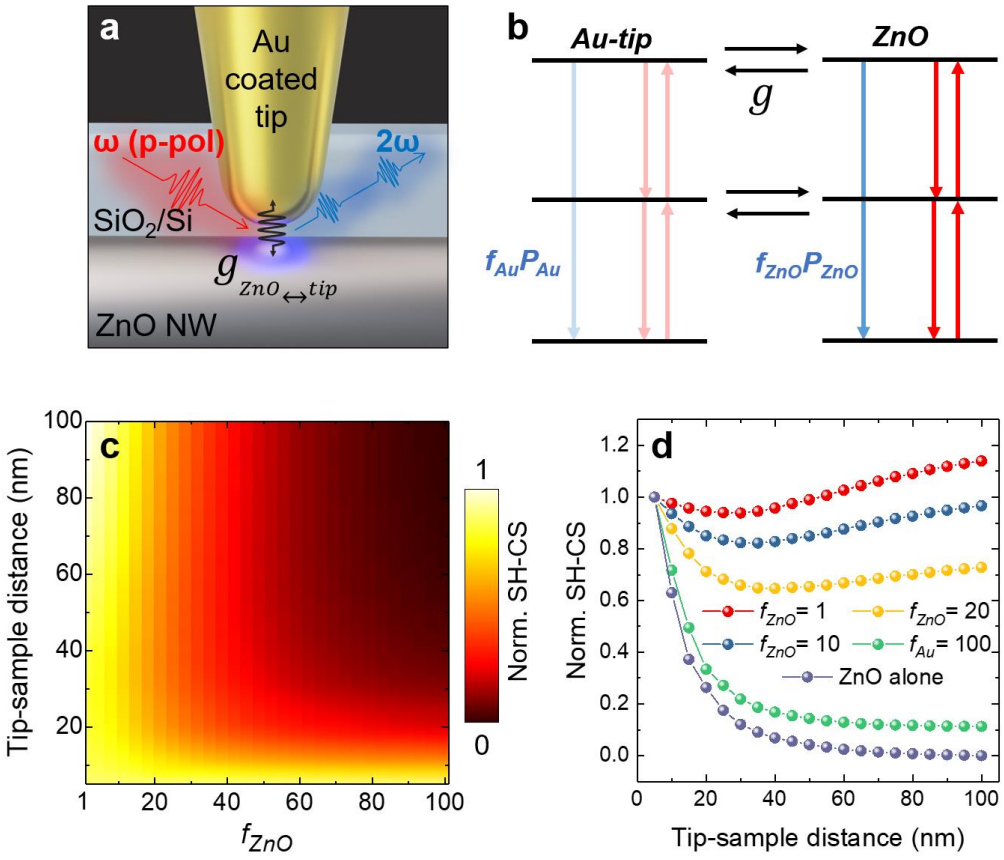

Figure 3: a) Schematic illustration of NET process between SHG-active Au coated tip and ZnO NW, showing near-field resonant energy transfer coefficient ($g_{ZnO\leftrightarrow tip}$). b) Three level energy transition structures of Au tip and ZnO NW, and Au- and ZnO-SHG enhancement factors, f_{Au} and f_{ZnO} with g. The red (blue) arrows indicate excitation or relaxation of photon energies by fundamental frequency, ω (SH frequency, 2ω). c) Simulated SH-CS of the Au tip according to different tip-sample distance (from 5 nm to 100 nm), and f_{ZnO} (from 1 to 100), while f_{Au} is fixed to unity. The SH-CS values are normalized to the value at 5 nm of tip-sample distance at each f_{ZnO}. d) Line profiles of normalized SH-CS according to tip-sample distance of the Au tip, showing the cases when f_{ZnO} is 1, 10, 20, and 100, while f_{Au} fixed to unity (extracted from panel c)), and the case when f_{Au}=0, indicating only the SHG property of ZnO NW ($\mathbf{P}_{ZnO}^{(2\omega)}$) is considered (purple).

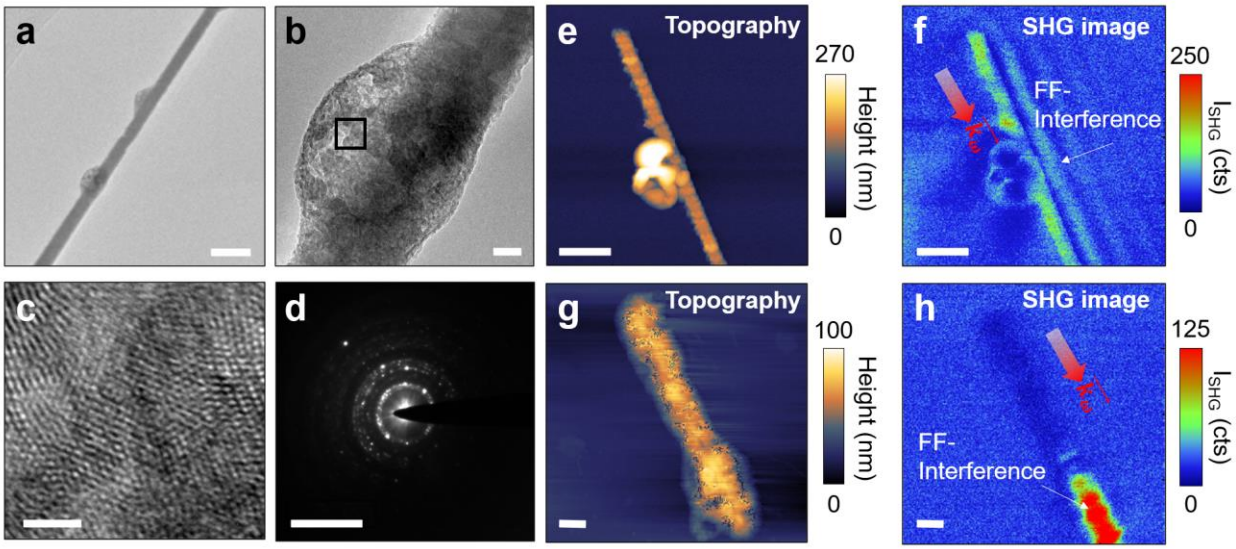

Figure 4: TEM analysis obtained from corroded ZnO NW: a) low magnification TEM image of overall corroded ZnO NW, b) HRTEM images of bubbled structure, c) magnified image, and d) SAED pattern. Panels c) and d) were taken from the square area in panel b), indicating polycrystalline nanostructure. The scale bars in panels a-d) indicate 200 nm, 20 nm, 2 nm, and 10 1/nm, respectively. e-h) Topography and near-field SHG images of moderately corroded (panels e) and f)) and heavily corroded (panels g) and h)) ZnO NWs. The scale bars are 1 μm.

Table of Contents (TOC)